Current Zero-Crossing Prediction-Based Critical Conduction Mode Control of Totem-Pole PFC Rectifiers

Mingde Zhou, *Student Member, IEEE*, Chuhan Peng, *Student Member, IEEE*, Junrui Liang, *Senior Member, IEEE*, Minfan Fu, *Senior Member, IEEE*, and Haoyu Wang, *Senior Member, IEEE*

***Abstract*—Critical conduction mode (CRM) is widely used in totem-pole Boost power factor correction converters due to its compatibility with soft-switching and high switching frequency. Conventionally, a current sensor or zero-current detector is required to realize CRM operation. The system performances highly rely on the behaviors of peripheral circuits. Additional power loss and delay are also introduced. Moreover, the inductor current contains obvious differential mode noise, which brings interferences to the sensing signals. To address this issue, a novel CRM realization method is proposed. It utilizes an inductor current estimator model to estimate the averaged current and to predict the current zero crossings. The noisy sensing signal is replaced by estimated values. Therefore, the zero-current detection circuit is removed, which simplifies the peripheral circuit design. Valley switching and zero-voltage switching can also be achieved. Operation principles, digital implementation, and error suppression of the proposed control are analyzed. The proposed concepts are validated on a 550-W, 150kHz − 1.6MHz, GaN-based prototype. Experimental results record 98.96% peak efficiency with a 0.9972 power factor.**

***Index Terms*—Critical conduction mode (CRM), current zero-crossing prediction, power factor correction (PFC), totem-pole.**

I. Introduction

POWER factor correction (PFC) converters are widely used in applications such as telecommunication power supplies and battery chargers [1]. Boost and its derived topologies dominate in ac/dc PFC converters [2]. Among them, totem-pole Boost topology outperforms with low components count, simple structure, and bidirectional power flow [3], [4], [5].

TABLE I
Comparison of CCM, DCM, and CRM

Mode	Current stress	Soft switching	Power level
CCM	Low	no	High
DCM	High	ZCS-on	Low
CRM	Medium	Valley-switching/ ZVS-on	Medium

In totem-pole Boost converters, continuous conduction mode (CCM), discontinuous conduction mode (DCM), and critical conduction mode (CRM) are three major operation modes. Table I summarizes the features of CCM, DCM, and CRM. As indicated, CCM provides low conduction loss but suffers from severe diode reverse recovery and high MOSFET turning-ON loss. DCM mitigates the diode reverse recovery by zero-current-switching (ZCS) with simple structure and control [6]. However, the power rating is limited. It is preferred to be used at light load when the conduction loss is nondominant. In comparison, CRM facilitates the MOSFET zero-voltage-switching (ZVS) or valley-switching turning-ON using quasi-resonant technique [7]. At higher power levels, CRM is preferred to DCM as its backflow current is negligible [8], [9]. Therefore, CRM is considered the optimal solution in medium power applications.

In CRM operation of totem-pole Boost converters, the zero-current detection (ZCD) circuit is widely employed [10], [11], [12], [13], [14]. The ZCD circuit locates the inductor current zero crossings when the switching loss is minimum [10], [11]. As a standing point, many derivative works are investigated to improve the power factor and efficiency performances. In [12], two phases are interleaved to mitigate the input filter attenuation requirement. In [13], by controlling the ON-time of the switch in the synchronous rectifier (SR), predictive ZVS and limited switching frequency can be realized. In [14], harmonic injection is utilized to optimize the switching frequency range. A ZCD signal is generated by comparing a current sensing signal with zero. However, few low-cost hall current sensors are available beyond hundreds of kHz.

Manuscript received 27 October 2022; revised 17 January 2023 and 9 March 2023; accepted 17 March 2023. Date of publication 21 March 2023; date of current version 19 May 2023. This work was supported in part by the National Natural Science Foundation of China under Grant 52077140, and in part by the Shanghai Rising Star Program under Grant 20QA1406700. Recommended for publication by Associate Editor S. Kapat. *(Corresponding author: Haoyu Wang.)*

Mingde Zhou is with the Power Electronics and Renewable Energies Laboratory and School of Information Science and Technology, ShanghaiTech University, Shanghai 201210, China, also with the Shanghai Institute of Microsystem and Information Technology, Chinese Academy of Sciences, Shanghai 200050, China, and also with the University of Chinese Academy of Sciences, Beijing 100049, China (e-mail: zhoumd@shanghaitech.edu.cn).

Chuhan Peng, Junrui Liang, Minfan Fu, and Haoyu Wang are with the School of Information Science and Technology, ShanghaiTech University, Shanghai 201210, ChinaShanghai Engineering Research Center of Energy Efficient and Custom AI IC, ShanghaiTech University, Shanghai 201210, China (e-mail: pengchh2022@shanghaitech.edu.cn; liangjr@shanghaitech.edu.cn; fumf@shanghaitech.edu.cn; wanghy@shanghaitech.edu.cn).

Color versions of one or more figures in this article are available at https://doi.org/10.1109/TPEL.2023.3259984.

Digital Object Identifier 10.1109/TPEL.2023.3259984

At high frequencies, current shunts and transformers are commonly used. Current shunt solutions have the advantage of high current sensing bandwidth [10], [11], [12], [13]. However, the inductor current shape tends to be distorted by the resistive shunt. This leads to a degraded total harmonic distortion (THD). In [15], Shahzad et al. adopt a small sensing resistor to reduce the negative effect and utilize an op-amp to amplify the current signal, which requires additional components. In [16], the current loop is compensated for the resistive part in the plant model of the converter. Meanwhile, to improve the sensing signal immunity, a hysteretic comparative window is introduced and generates a time delay between the ZCD signal and the current zero-crossing point, which affects the performance [17]. In [18], an auxiliary winding is coupled with the boost inductor. ZCD signal is captured when the boost inductor's voltage commutates to positive. In [19], the maximum voltage drop on the secondary windings is limited by a saturable core. The conduction loss is reduced compared with the shunt solutions. However, the transformer cores are bulky and the time delay of ZCD still exists.

To overcome the limitations of the ZCD circuits, ZVS-catch methods are developed in [20] and [21]. It directly senses the drain–source voltage and detects its zero-crossing point. However, this method is demanding in the circuit design due to the switching noise from the drain–source voltage. In [20], this method is first applied with on-chip design. In [21], the board stage realization is achieved with a novel diode-clamped circuit.

Increasing the current ripple on the CCM designs can also achieve CRM operation [22], [23], [24], [25]. In [22], a high-speed current sensor is utilized in the feedback loop and the inductor current ripple is directly controlled. In [23], [24], and [25], a frequency modulation method is used to inject a programmed current ripple into the boost inductor current. The performance of these methods relies on the current loop. However, large differential mode noise exists on the inductor current sensing signals [26]. This mainly attributes to the CRM operation. The frequency response of the current sensor also introduces additional phase offsets at high frequencies.

To avoid the usage of inaccurate current sensing signals, many predictive current sensorless control methods are developed for PFC converters [27], [28], [29]. Accordingly, the advantages of CRM over CCM in terms of high conversion efficiency and simple control are further highlighted. However, removing both the current sensor and the ZCD/ZVS catch circuit makes the control more challenging. Moreover, these reported methods mainly focus on CCM control under small current ripple assumptions. In CRM scenarios, large current ripples deteriorate the accuracy of the averaged inductor current model.

In this article, a current zero-crossing prediction-based CRM control is proposed for the totem-pole PFC rectifier. The major research contributions include the following.

1) A novel current estimator is proposed for CRM control. The behaviors of the estimator considering the nonlinear output capacitance of switching devices are modeled and analyzed.
2) The proposed current estimator predicts the inductor's current zero-crossing points. Thus, conventional ZCD circuit is removed. This reduces the component count of the peripheral circuits and the resistive losses in the power circuit. Moreover, to improve the prediction performance, a disturbance damping control is proposed to mitigate the variation of inductance and parasitic resistance.
3) Conventional double-loop control scheme is simplified. The proposed current estimator provides information on both the instant current and average current. The noisy CRM current signal is excluded from the control loop.
4) High power factor and high efficiency can be realized simultaneously. No current sensor, ZCD circuit, or ZVS-catch circuits are required. Valley switching and zero-voltage switching are achieved.
5) The proposed concept is naturally compatible with high-frequency GaN devices.

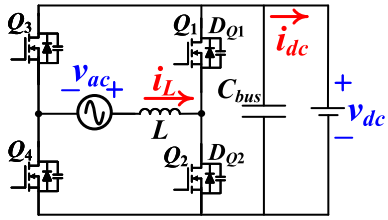

Fig. 1. Schematic of the totem pole Boost PFC converter.

The rest of this article is organized as follows. Section II introduces the operating principles of the CRM totem-pole converter. The proposed current estimator with zero-current prediction is derived in Section III. The proposed estimator-based CRM control is detailed in Section IV. In Section V, experimental results are demonstrated. Finally, Section VI concludes this article.

II. Steady-State Analysis of CRM Operation

A typical single-phase totem-pole Boost PFC rectifier is illustrated in Fig. 1. It contains two high-frequency switches Q_1, Q_2, two low-frequency switches Q_3, Q_4, and a Boost inductor L. D_{Q1} and D_{Q2} are body diodes of Q_1 and Q_2, respectively. i_L is the current of L. $v_{\rm ac}$ is the input ac voltage. $C_{\rm bus}$ is the filtering capacitor on the dc-link. $v_{\rm dc}$ is the dc-link voltage.

The positive half-cycle can be divided into seven operation states as shown in Fig. 2. The negative half-cycle is similar. Since the switching frequency is much higher than line frequency, $v_{\rm dc}$, $v_{\rm ac}$ can be considered as constants over one specific switching cycle.

According to whether D_{Q1} conducts, the circuit operation can be divided into two categories, as shown in Figs. 3 and 4. In the normal power transfer scenario, D_{Q1} conducts. Once D_{Q1} conducts, there is a positive power flowing into the dc-link. In the nonpower transfer scenario, only circulating power exists.

A. Normal Power Transfer Scenarios

Typical waveforms of the normal power transfer scenario are shown in Fig. 3. t_0, t_4, and t_7 are current zero-crossing instants.

1) State I*:* t_0–t_1*:* During this time interval, the circuit is in State I. The voltage across L is $v_{\rm ac}$. i_L increases linearly as

$$i_L = \frac{v_{\rm ac}}{L}(t - t_0). \tag{1}$$

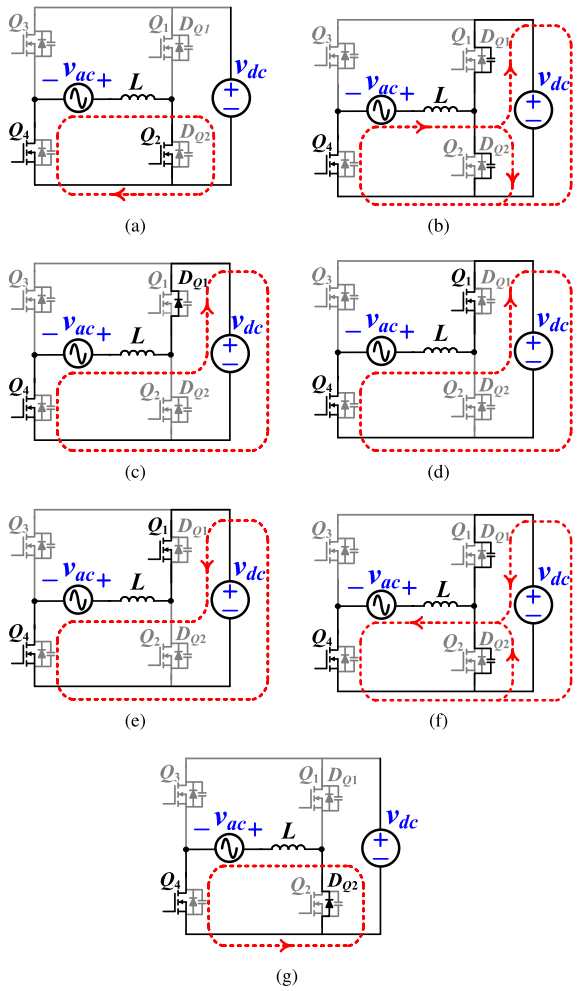

Fig. 2. Operation states in positive half line cycle. (a) State I. (b) State II. (c) State III. (d) State IV. (e) State V. (f) State VI. (g) State VII.

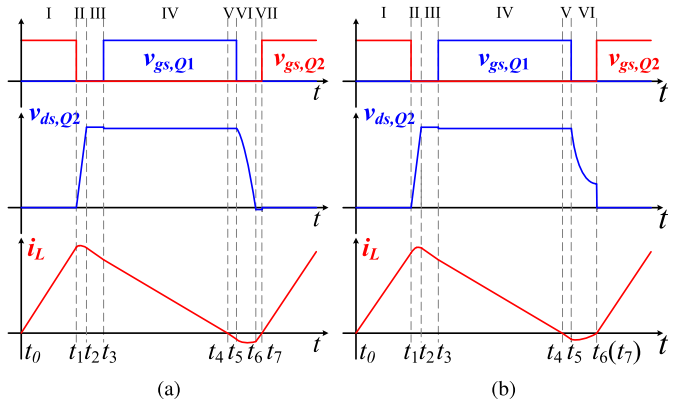

Fig. 3. Typical waveforms of gate signals, drain-source voltage, and the inductor current in CRM operation for normal power transfer scenarios. (a) ZVS case. (b) Valley-switching case.

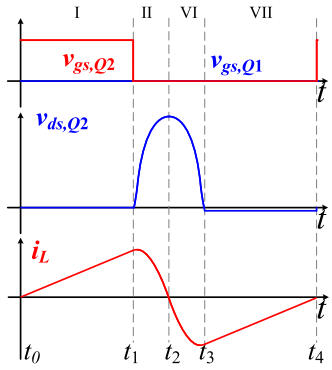

Fig. 4. Typical gate signals, drain–source voltage, and the inductor current in CRM operation for nonpower transfer scenarios.

2) State II*:* t_1–t_2*:* The circuit is in State II. $C_{\rm oss}$ of Q_1 and Q_2 resonates with L. When D_{Q1} conducts at t_2, this state ends. The ZVS condition for Q_1 is created. The characteristic impedance (Z_n) and resonant frequency (ω_n) are

$$Z_n = \sqrt{\frac{L}{2C_{\rm oss}}}, \omega_n = \frac{1}{\sqrt{2C_{\rm oss}L}}.$$

Drain–source voltage of Q_2 ($v_{{\rm ds},Q2}$) and i_L yield to the second-order transient response.

$$v_{{\rm ds},Q2} = v_{\rm ac} + Z_n i_L(t_1)\sin\left[\omega_n(t-t_1)\right] - v_{\rm ac}\cos\left[\omega_n(t-t_1)\right] \quad (2)$$

$$i_L = \frac{v_{\rm ac}}{Z_n}\sin\left[\omega_n(t-t_1)\right] + i_L(t_1)\cos\left[\omega_n(t-t_1)\right]. \quad (3)$$

3) State III*:* t_2–t_3*:* During this time interval, the circuit is in State III. D_{Q1} conducts with a voltage drop V_D. This state ends when the gate signal of Q_1 rises. i_L linearly decreases as

$$i_L = i_L(t_2) + \frac{v_{\rm ac} - v_{\rm dc} - V_D}{L}(t-t_2). \quad (4)$$

4) State IV*:* t_3–t_4*:* When the SR is enabled at t_3, the circuit enters into State IV. Q_1 is turned ON such that i_L flows through the MOSFET channel. i_L decreases linearly. At t_4, i_L crosses zero.

$$i_L = i_L(t_3) + \frac{v_{\rm ac} - v_{\rm dc}}{L}(t-t_3). \quad (5)$$

5) State V*:* t_4–t_5*:* During this time interval, the circuit is in State V. i_L flows back to the source $v_{\rm ac}$. This state ends at t_5 when the gate signal of Q_1 changes to zero.

$$i_L = \frac{v_{\rm ac} - v_{\rm dc}}{L}(t-t_4) \quad (6)$$

6) State VI*:* t_5–t_6*:* $C_{\rm oss}$ resonates with L in State VI. At t_6, $v_{{\rm ds},Q2}$ reaches its valley, which creates a ZVS or valley-switching condition for Q_2. In ZVS conditions, this state ends at t_6, as shown in Fig. 3(a). For some scenarios, $v_{{\rm ds},Q2}$ never hits zero. Then, this state ends at t_7, which corresponds to the valley point, as demonstrated in Fig. 3(b). $v_{{\rm ds},Q1}$ and i_L yield

$$v_{{\rm ds},Q1} = v_{\rm dc} - v_{\rm ac} - (v_{\rm dc} - v_{\rm ac})\cos\left[\omega_n(t-t_5)\right] - Z_n i_L(t_5)\sin\left[\omega_n(t-t_5)\right] \quad (7)$$

$$i_L = \frac{v_{\rm ac} - v_{\rm dc}}{Z_n}\sin\left[\omega_n(t-t_5)\right] + i_L(t_5)\cos\left[\omega_n(t-t_5)\right] \quad (8)$$

ZVS of Q_2 can be realized if $v_{ac} \leq 0.5v_{dc}$. Otherwise the ZVS condition depends on $i_L(t_5)$. If $i_L(t_5)$ is close to zero, valley switching is realized, $t_6 = t_7$.

The differences between states II and VI mainly lie in the initial condition and ZVS or valley-switching energy source. In State II, the ZVS energy comes from the ac source. While in State VI, the ZVS or valley-switching energy comes from the dc-link.

7) State VII*:* t_6–t_7*:* During this period, i_L increases linearly. The circuit is in State VII. D_{Q2} conducts. This state ends at t_7 when i_L hits zero. Another switching cycle starts at t_7. i_L is

$$i_L = i_L(t_6) + \frac{v_{ac} + V_D}{L}(t - t_6). \tag{9}$$

B. Nonpower Transfer Scenarios

In some scenarios, the peak i_L is insufficient to fully charge the C_{oss} of Q_1. Therefore, $v_{ds,Q1}$ never falls below zero. Hence, Q_1 is kept OFF. Then, states III, IV, and V do not exist. The converter works in nonpower transfer scenarios. Typical waveforms in the nonpower transfer scenarios are demonstrated in Fig. 4.

1) State I*:* t_0–t_1*:* The circuit is in State I. i_L linearly increases. The state ends at t_1. i_L is as follows:

$$i_L = \frac{v_{ac}}{L}(t - t_0). \tag{10}$$

2) State II*:* t_1–t_2*:* The circuit is in State II. C_{oss} of Q_1 and Q_2 resonates with L. This state ends when i_L crosses zero at t_2. $v_{ds,Q2}$ and i_L are derived

$$v_{ds,Q2} = v_{ac} + Z_n i_L(t_1)\sin\left[\omega_n(t - t_1)\right] - v_{ac}\cos\left[\omega_n(t - t_1)\right] \tag{11}$$

$$i_L = \frac{v_{ac}}{Z_n}\sin\left[\omega_n(t - t_1)\right] + i_L(t_1)\cos\left[\omega_n(t - t_1)\right]. \tag{12}$$

3) State VI*:* t_2–t_3*:* The circuit is in State VI. C_{oss} of Q_1 and Q_2 resonates with L. This state ends when D_{Q2} conducts at t_3. $v_{ds,Q2}$ and i_L are derived

$$v_{ds,Q2} = v_{ac} + v_{ac}\sin\left[\omega_n(t - t_2) + \arctan\frac{v_{ac}}{Z_n i_L(t_1)}\right] + Z_n i_L(t_1)\cos\left[\omega_n(t - t_2) + \arctan\frac{v_{ac}}{Z_n i_L(t_1)}\right] \tag{13}$$

$$i_L = \frac{v_{ac}}{Z_n}\cos\left[\omega_n(t - t_2) + \arctan\frac{v_{ac}}{Z_n i_L(t_1)}\right] - i_L(t_1)\sin\left[\omega_n(t - t_2) + \arctan\frac{v_{ac}}{Z_n i_L(t_1)}\right]. \tag{14}$$

In States II and VI of nonpower transfer scenario, the time interval $t_3 - t_1$ is longer than half the resonant period, $t_3 - t_1 = [\pi + 2\arctan(v_{ac}/i_L(t_1)/Z_n)]/\omega_n$.

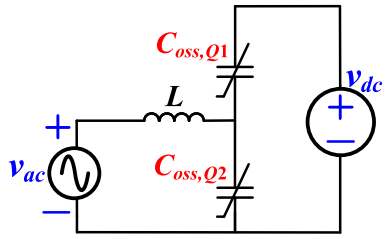

Fig. 5. Equivalent resonant circuit in the deadband with nonlinear capacitance of Q_1 and Q_2.

4) State VII*:* t_3–t_4*:* The circuit is in State VII. During this time interval, i_L increases linearly. D_{Q2} conducts. This state ends at t_4 when i_L hits zero. Another switching cycle starts at t_4. i_L is expressed as

$$i_L = i_L(t_4) + \frac{v_{ac} + V_D}{L}(t - t_6). \tag{15}$$

III. Proposed Current Estimator Model

To avoid the limitations of current sensors and ZCD circuits in CRM control, an accurate current estimator model is required to predict the current zero-crossing points. In CRM, the current ripple is high and resonance may occur in the deadband. This brings challenges to the modeling of current estimator. In [30], C_{oss} is modeled as a time-related capacitor to calculate i_L in (3) and (8). The model has satisfied accuracy in estimating the ZVS or valley-switching time and the peaks or valleys of the current during the resonance. However, C_{oss} exhibits high nonlinearity and brings errors to the current estimation and zero-crossing prediction [31]. To cope with this issue, we propose a novel current estimator model. In this model, the charge exchanged during the deadband is utilized to estimate i_L, and the time-related capacitor is utilized to calculate ZVS or valley-switching condition.

A. Deadband Resonance Analysis

The accuracy of the current estimator affects the PFC performance. Behaviors of the estimator imitate the i_L model. Nonlinear C_{oss} makes the conventional model inaccurate for i_L estimation in the deadband. Therefore, the deadband resonance considering the nonlinearity is investigated in this section, as illustrated in Fig. 5.

In nonpower transfer case, the symmetrical characteristics of i_L in the deadband have been analyzed in the previous section. Therefore, this section focuses on the analysis of i_L during normal power transmission. The following model takes into account the nonlinear characteristics of C_{oss}, as shown in Fig. 6. C_{oss} in Fig. 6(a) is extracted from the datasheet. The stored charge in Fig. 6(b) is obtained by integrating C_{oss} over v_{ds}. Fig. 6(c) shows the sum of $E_{oss,Q1}$ and $E_{oss,Q2}$, where E_{oss} is the stored energy in the corresponding transistor.

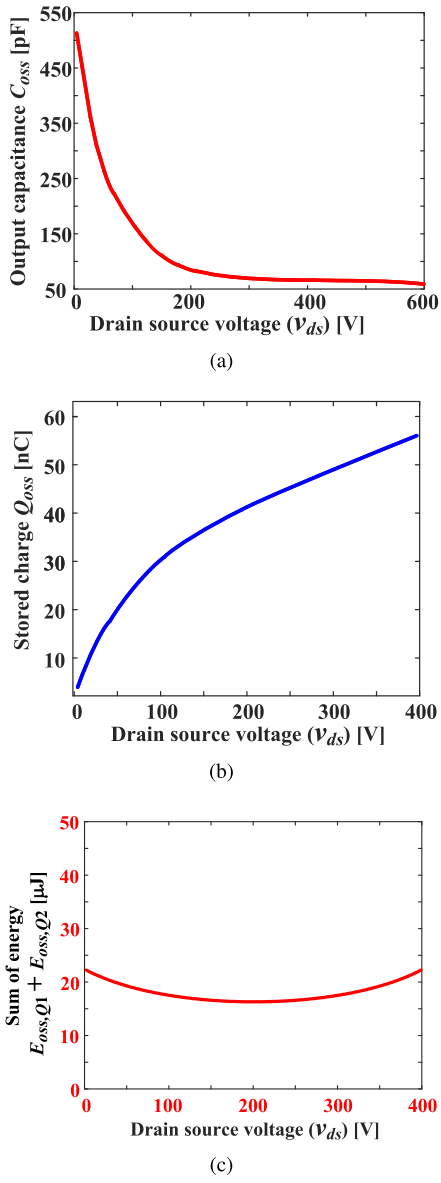

Fig. 6. Relationship between drain–source voltage $v_{\text{ds},Q2}$ and (a) C_{oss}, (b) Q_{oss}, and (c) sum of output capacitance energy $E_{\text{oss},Q1} + E_{\text{oss},Q2}$.

1) State II $t_1 \sim t_2$: In State II, $C_{\text{oss},Q2}$ is charged and $C_{\text{oss},Q1}$ is discharged. $Q_{\text{top},f}$ and $Q_{\text{bot},f}$ are noted as the charge exchanged in Q_1 and Q_2 during this process, respectively.

$$\begin{aligned} Q_{\text{top},f} &= -\int_{t_1}^{t} i_{\text{ds},Q1}dt \\ &= Q_{\text{oss}}(v_{\text{dc}}) - Q_{\text{oss}}(v_{\text{dc}} - v_{\text{ds},Q2}(t)) \\ Q_{\text{bot},f} &= \int_{t_1}^{t} i_{\text{ds},Q2}dt = Q_{\text{oss}}(v_{\text{ds},Q2}(t)). \end{aligned} \tag{16}$$

According to energy conservation

$$\begin{aligned} &\frac{1}{2}Li_L^2(t_1) + (Q_{\text{top},f} + Q_{\text{bot},f})v_{\text{ac}} + E_{\text{oss},Q1}(t_1) + E_{\text{oss},Q2}(t_1) \\ &= \frac{1}{2}Li_L^2(t) + v_{\text{dc}}Q_{\text{top},f} + E_{\text{oss},Q1}(t) + E_{\text{oss},Q2}(t). \end{aligned} \tag{17}$$

At t_1, $v_{\text{ds},Q2} = 0$. At t_2, $v_{\text{ds},Q2} = v_{\text{dc}}$. According to Fig. 6(c), $E_{\text{oss},Q1}(t_1) + E_{\text{oss},Q2}(t_1) = E_{\text{oss},Q1}(t_2) + E_{\text{oss},Q2}(t_2)$. Hence, the equation can be rewritten as follows:

$$\begin{aligned} &\frac{1}{2}Li_L^2(t_1) + [Q_{\text{top},f}(t_2) + Q_{\text{bot},f}(t_2)]v_{\text{ac}} \\ &= \frac{1}{2}Li_L^2(t_2) + v_{\text{dc}}Q_{\text{top},f}(t_2). \end{aligned} \tag{18}$$

At t_2, i_L is derived as

$$\begin{aligned} &i_L(t_2) \\ &= \sqrt{i_L(t_1)^2 + \frac{2}{L}\left[Q_{\text{top},f}(t_2)(v_{\text{ac}} - v_{\text{dc}}) + Q_{\text{bot},f}(t_2)v_{\text{ac}}\right]}. \end{aligned} \tag{19}$$

2) State VI $t_5 \sim t_6$: In State VI, $C_{\text{oss},Q1}$ is charged and $C_{\text{oss},Q2}$ is discharged. $Q_{\text{top},r}$ and $Q_{\text{bot},r}$ are noted as the charge exchanged in Q_1 and Q_2 during this process, respectively.

$$\begin{aligned} Q_{\text{top},r} &= -\int_{t_5}^{t} i_{\text{ds},Q1}dt \\ &= -Q_{\text{oss}}(v_{\text{dc}} - v_{\text{ds},Q2}(t)) \\ Q_{\text{bot},r} &= \int_{t_5}^{t} i_{\text{ds},Q2}dt \\ &= Q_{\text{oss}}(v_{\text{ds},Q2}(t)) - Q_{\text{oss}}(v_{\text{dc}}). \end{aligned} \tag{20}$$

In the valley-switching case, the current at t_6 is zero [32]. The remained energy at t_6 is dissipated in the GaN HEMT 2DEG [33].

In the ZVS case, according to energy conservation

$$\begin{aligned} &\frac{1}{2}Li_L^2(t_5) + (Q_{\text{top},r} + Q_{\text{bot},r})v_{\text{ac}} + E_{\text{oss},Q1}(t_5) + E_{\text{oss},Q2}(t_5) \\ &= \frac{1}{2}Li_L^2(t) + v_{\text{dc}}Q_{\text{top},r} + E_{\text{oss},Q1}(t) + E_{\text{oss},Q2}(t). \end{aligned} \tag{21}$$

At t_5, $v_{\text{ds},Q2} = v_{\text{dc}}$. At t_6, $v_{\text{ds},Q2} = 0$. According to Fig. 6(c), $E_{\text{oss},Q1}(t_5) + E_{\text{oss},Q2}(t_5) = E_{\text{oss},Q1}(t_6) + E_{oss,Q2}(t_6)$. Hence, (21) can be rewritten as

$$\begin{aligned} &\frac{1}{2}Li_L^2(t_5) + (Q_{\text{top},r}(t_6) + Q_{\text{bot},r}(t_6))v_{\text{ac}} \\ &= \frac{1}{2}Li_L^2(t_6) + v_{\text{dc}}Q_{\text{top},r}(t_6). \end{aligned} \tag{22}$$

Considering both ZVS and valley-switching cases, at t_6, i_L is derived as (23) shown at the bottom of next page.

B. Current Zero-Crossing Prediction

The ON-time (T_{on}) counts from i_L zero-crossing point t_0 and ends at t_1. $T_{\text{on}} = t_1 - t_0$. The estimated inductor current ($i_{L,\text{est}}$) at the end of T_{on} is

$$i_{L,\text{est}}(t_1) = \frac{v_{\text{ac}}}{L}T_{\text{on}}. \tag{24}$$

The criteria for entering the nonpower transfer scenario relies on $i_L(t_1)$. i_L variation is estimated following the principle of energy conservation in the interval $t_1 \sim t_2$. If Q_1 can achieve ZVS turning-ON, the circuit works in normal power transfer scenario.

The following equation holds:

$$\frac{1}{2}Li_L^2(t_1)+2Q_{\text{tot}}v_{\text{ac}}=\frac{1}{2}Li_L^2(t_2)+v_{\text{dc}}Q_{\text{tot}} \tag{25}$$

where Q_{tot} is the overall charge flowing through a single switch (Q_1 or Q_2) when its drain–source voltage rises from 0 to v_{dc}, $Q_{\text{tot}}\equiv Q_{\text{oss}}(v_{\text{dc}})$.

If $v_{\text{ac}}>(v_{\text{dc}}-v_{\text{ac}})$, (25) holds and $i_{L1}(t_2)>i_{L1}(t_1)$. $i_L(t_2)$ is always sufficient to enable the ZVS turning-ON of Q_1. However, when $i_L^2(t_1)<-2K_1$, $K_1=Q_{\text{tot}}(2v_{\text{ac}}-v_{\text{dc}})/L$, (25) does not hold and D_{Q1} never conducts. The circuit works in nonpower transfer scenario.

Hence, $i_{L,\text{est}}$ at t_2 is derived as follows:

$$i_{L,\text{est}}(t_2)=\begin{cases}\sqrt{i_{L,\text{est}}^2(t_1)+2K_1}, & T_{\text{on}}^2>-2K_1L^2/v_{\text{ac}}^2\\ 0, & T_{\text{on}}^2\le -2K_1L^2/v_{\text{ac}}^2\end{cases} \tag{26}$$

$i_{L,\text{est}}(t_2)$ are different in normal power transfer scenario and nonpower transfer scenario, the current estimator runs in different cases.

1) Normal Power Transfer Scenario: The charge flow in the resonance $t_1\sim t_2$ is very fast in the normal power transfer scenario. The resonant duration $T_{\text{res},1}=t_2-t_1$ is estimated by a trapezoid approximation as shown in Fig. 3(a).

$$T_{\text{res},1}=\frac{4Q_{\text{tot}}}{i_{L,\text{est}}(t_2)+i_{L,\text{est}}(t_1)}. \tag{27}$$

The error between the actual deadtime $T_{\text{res},1,\text{act}}$ and the approximated value $T_{\text{res},1}$ at both light-load and full-load conditions are evaluated in Fig. 8. $T_{\text{res},1,\text{act}}$ is achieved from simulation results considering the nonlinear $C_{\text{oss}}-v_{\text{ds}}$ properties.

As shown in Fig. 8(a), the error decreases with the increase of power. At light load (150 W), the estimated $T_{\text{res},1}$ has a difference within 40 ns compared with the actual $T_{\text{res},1,\text{act}}$. The estimation error decreases with the increase of inductor current. From Fig. 8(b), due to the minimum DSP EPWM step in the deadband, the difference between $T_{\text{res},1,\text{act}}$ and $T_{\text{res},1}$ at full load condition is within 5 ns. When the average inductor current rises, the error decreases. Therefore, the accuracy of the trapezoid approximation in (27) is acceptable.

The inductor current in $t_2\sim t_5$ is decreasing. $T_{d,f}$ is the deadband set by the controller after the active switch turns OFF. $T_{d,f}$ should be longer than $T_{\text{res},1}$.

$$T_{d,f}=(t_3-t_1)\ge T_{\text{res},1}. \tag{28}$$

T_{SR} is the SR switch conducting time, $T_{\text{SR}}=(t_5-t_3)$. $i_{L,\text{est}}(t_5)$ is calculated as follows:

$$i_{L,\text{est}}(t_5)=i_{L,\text{est}}(t_2)+\frac{v_{\text{ac}}-v_{\text{dc}}}{L}T_{\text{SR}}+\frac{v_{\text{ac}}-v_{\text{dc}}-V_D}{L}(T_{d,f}-T_{\text{res},1}). \tag{29}$$

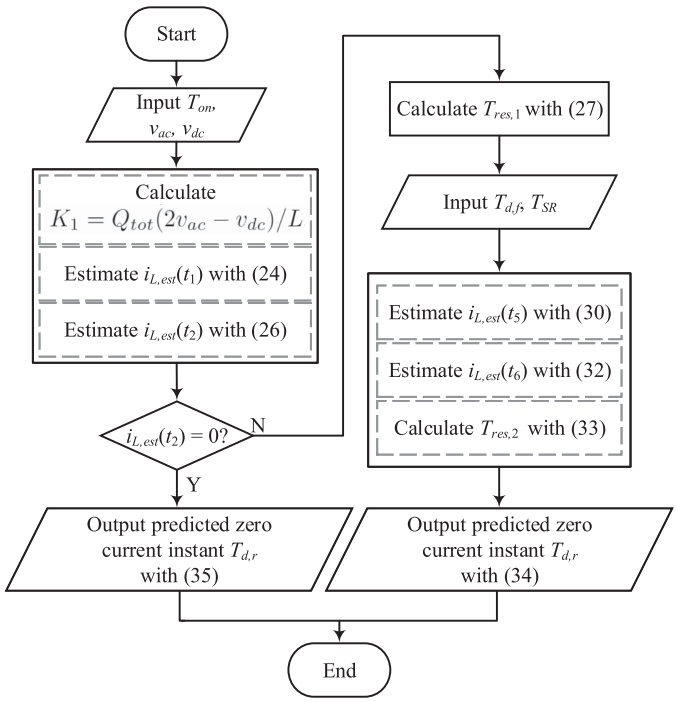

Fig. 7. Flowchart of the proposed current zero-crossing prediction algorithm.

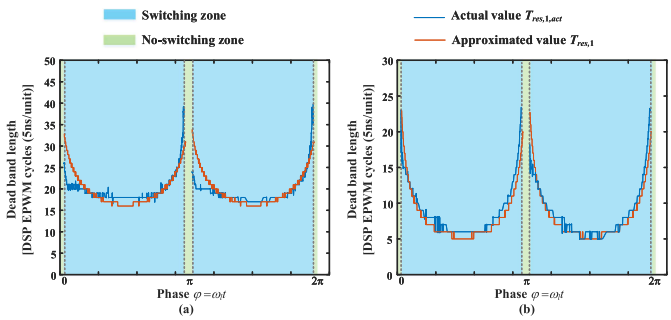

Fig. 8. Comparison between the actual deadtime $T_{\text{res},1,\text{act}}$ and the approximated deadtime $T_{\text{res},1}$ at (a) light load (150 W) and (b) full load.

Since $v_{\text{dc}}-v_{\text{ac}}\gg V_D$, (29) can also be approximated as follows:

$$i_{L,\text{est}}(t_5)=i_{L,\text{est}}(t_2)+\frac{v_{\text{ac}}-v_{\text{dc}}}{L}(T_{\text{SR}}+T_{d,f}-T_{\text{res},1}). \tag{30}$$

During $t_5\sim t_6$, L resonates with the nonlinear C_{oss}. With energy conservation, the following equation yields:

$$\frac{1}{2}Li_L^2(t_5)+v_{\text{dc}}Q_{\text{tot}}=\frac{1}{2}Li_L^2(t_6)+2Q_{\text{tot}}v_{\text{ac}}. \tag{31}$$

When $v_{\text{ac}}<0.5v_{\text{dc}}$, ZVS of Q_2 can be realized with a negative $i_L(t_6)$. Otherwise, the ZVS condition is determined by $i_L(t_5)$. If (31) does not hold, valley switching is achieved, and ZVS is

$$i_L(t_6)=\begin{cases}\sqrt{i_L(t_5)^2+\frac{2}{L}[Q_{\text{top},r}(t_6)(v_{\text{ac}}-v_{\text{dc}})+Q_{\text{bot},r}(t_6)v_{\text{ac}}]}, & \text{ZVS case}\\ 0, & \text{Valley}-\text{switching case.}\end{cases} \tag{23}$$

lost. $i_{L,\text{est}}$ at t_6 is derived as

$$i_{L,\text{est}}(t_6)=\begin{cases}-\sqrt{i_{L,\text{est}}^2(t_5)-2K_1}, & i_{L,\text{est}}^2(t_5)-2K_1>0\\ 0, & i_{L,\text{est}}^2(t_5)-2K_1\le 0.\end{cases} \tag{32}$$

Since the inductor current starts or ends near zero, trapezoid approximation is not accurate to estimate the deadband before the turning ON of Q_2. The resonance $T_{\text{res},2}=t_6-t_5$ in this zone is calculated via (7) and (8).

$$T_{\text{res},2}=\frac{\pi+\arctan\frac{i_{L,\text{est}}(t_5)Z_n}{v_{\text{dc}}-v_{\text{ac}}}+\arctan\frac{i_{L,\text{est}}(t_6)Z_n}{v_{\text{ac}}}}{\omega_n}. \tag{33}$$

During $t_6\sim t_7$, a freewheeling current flows through the equivalent body diode of Q_2. i_L follows (9). The deadband before the switch turning ON is $T_{d,r}$. The zero-current prediction is achieved by controlling $T_{d,r}$.

$$T_{d,r}=t_7-t_5=-i_{L,\text{est}}(t_6)\frac{L}{v_{\text{ac}}+V_D}+T_{\text{res},2}. \tag{34}$$

2) Nonpower Transfer Scenario: In the nonpower transfer scenario, the inductor resonates with C_{oss} of Q_1 and Q_2 during $t_1\sim t_3$. $v_{\text{ds},Q2}$ is the same at t_1 and t_3. Therefore, $i_L(t_3)=-i_L(t_1)$. Time parameters $T_{d,f},T_{\text{SR}},T_{d,r}$ are derived as

$$T_{d,f}=t_3-t_1=\frac{\pi+2\arctan\frac{L}{Z_nT_{\text{on}}}}{\omega_n}$$
$$T_{\text{SR}}=0, T_{d,r}=t_4-t_3=\frac{v_{\text{ac}}}{v_{\text{ac}}+V_D}T_{\text{on}}. \tag{35}$$

The entire process of the current zero-crossing prediction is illustrated in Fig. 7. With given T_{on}, v_{ac}, and v_{dc}, $i_{L,\text{est}}(t_1)$ and $i_{L,\text{est}}(t_2)$ are estimated. Then, if $i_{L,\text{est}}(t_2)>0$, the normal power transfer model is used to predict the zero-current instant. Otherwise, the nonpower transfer model is utilized.

C. Averaged Inductor Current Estimation

According to Fig. 4, the averaged inductor current $i_{L,\text{avg}}$ in the nonpower transfer zone is 0.

In the normal power transfer scenario, i_L has two resonance intervals. Therefore, it is difficult to accurately estimate the averaged current in real time based on simple calculations. On the other hand, the transient process is trivial compared with T_{on} or T_{SR}, the triangular approximation can be used to estimate the averaged inductor current. The peak current is approximated as $i_L(t_1)$. The valley current is derived via (8).

Taking both normal power transfer and nonpower transfer scenarios into consideration, the estimated averaged inductor current $i_{L,\text{avg,est}}$ is derived as

$$i_{L,\text{avg,est}}=\begin{cases}0, & T_{\text{on}}^2\le -2K_1L^2/v_{\text{ac}}^2\\ \frac{v_{\text{ac}}T_{\text{on}}Z_n-L(v_{\text{dc}}-v_{\text{ac}})}{2Z_nL}, & T_{\text{on}}^2>-2K_1L^2/v_{\text{ac}}^2.\end{cases} \tag{36}$$

The error between the averaged inductor current $i_{L,\text{avg,act}}$ and the triangular approximated current $i_{L,\text{avg,est}}$ has been evaluated at light load and full load in Fig. 9. $i_{L,\text{avg,act}}$ is achieved from simulation results considering the nonlinearity of $C_{\text{oss}}-v_{\text{ds}}$.

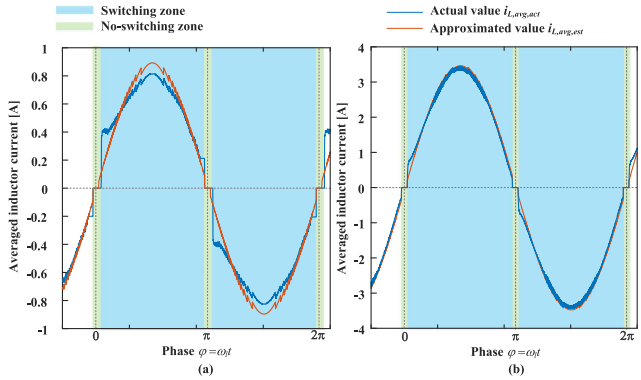

Fig. 9. Comparison between the averaged inductor current $i_{L,\text{avg,act}}$ and the triangular approximated current $i_{L,\text{avg,est}}$ at (a) light load (150 W) and (b) full load.

The current waveform comparison of $i_{L,\text{avg,act}}$ and $i_{L,\text{avg,est}}$ at light load is shown in Fig. 9(a). The triangular approximation is higher than the accurate value by 0.1 A at the peak current point. In Fig. 9(b), the triangular approximation is higher than the accurate value by 0.04 A at the peak current point. This error is relatively minor. Meanwhile, the approximation effectively relieves the computation burden. Indeed, calculating the averaged inductor current in real time is very complicated and time consuming. In the proposed method, triangular approximation achieves a good compromise between model accuracy and real-time execution.

The iTHD of $i_{L,\text{avg,act}}$, and $i_{L,\text{avg,est}}$ at light load (150 W) are 7.47% and 1.97%, respectively. The iTHD of $i_{L,\text{avg,act}}$ and $i_{L,\text{avg,est}}$ at full load are 4.17% and 1.65%, respectively. The S_3-S_4 commutation deadband (green zone) degrades the iTHD of $i_{L,\text{avg,est}}$. The approximation accuracy in the proposed method increases with the increase of power.

IV. Current Estimator-Based CRM PFC Control

A. Disturbance Damping

In PFC applications, disturbance from the inductance variation and parasitic resistance may inject distortion to the estimator, which brings error to the current zero-crossing prediction.

In Fig. 10, the inductor current waveforms in ideal and disturbed cases are plotted. Fig. 8(a) demonstrates the natural ZVS case and Fig. 8(b) illustrates the valley-switching case. Fig. 8 8(c) shows the ZVS extension case. The green dashed curve corresponds to the ideal case.

Ideally, SR should be turned OFF at $i_{\text{val1,ideal}}$.

$$i_{\text{val1,ideal}}=\begin{cases}0, & v_{\text{ac}}\le 0.5v_{\text{dc}}\\ 0, & v_{\text{ac}}>0.5v_{\text{dc}}\text{ with valley switching}\\ \sqrt{2K_1}, & v_{\text{ac}}>0.5v_{\text{dc}}\text{ with ZVS extension.}\end{cases} \tag{37}$$

Adding a disturbance Δi on the turning-OFF current gives the blue curve $i_{\text{val1}}(n)$.

$$i_{\text{val1}}(n)=i_{\text{val1,ideal}}+\Delta i. \tag{38}$$

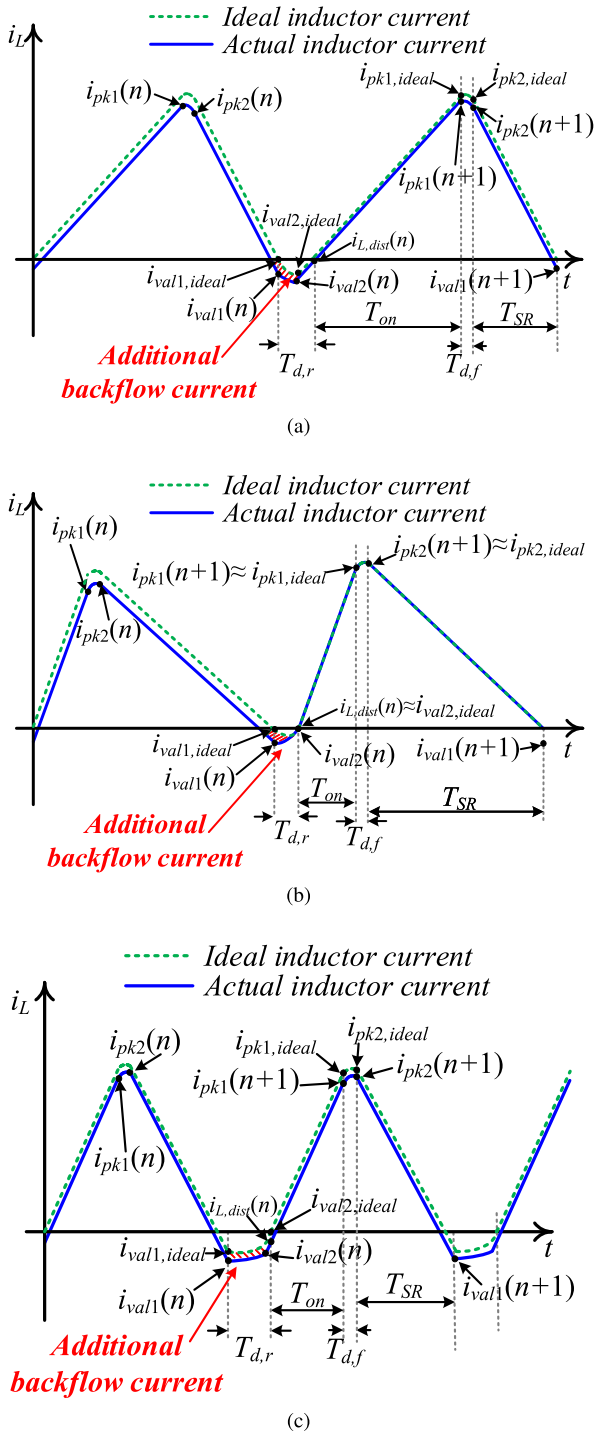

Fig. 10. Waveform with additional SR conduction time by minimum time length of DSP. (a) ZVS case. (b) Valley-switching case. (c) ZVS extension case.

In Fig. 10, the disturbance provides additional backflow current for ZVS of Q_2. During the resonance, the actual inductor current changes to $i_{\text{val2}}(n)$.

$$i_{\text{val2}}(n) \approx \begin{cases} -\sqrt{-2K_1 + i_{\text{val1}}^2(n)}, & K_1 < i_{\text{val1}}^2(n)/2 \\ 0, & K_1 \geq i_{\text{val1}}^2(n)/2. \end{cases} \tag{39}$$

Compared with the ideal current $i_{\text{val2,ideal}}$

$$i_{\text{val2,ideal}} = \begin{cases} -\sqrt{-2K_1}, & v_{\text{ac}} < 0.5v_{\text{dc}} \\ 0, & v_{\text{ac}} \geq 0.5v_{\text{dc}}. \end{cases} \tag{40}$$

The ideal peak current is approximated as twice the input averaged current. $V_{\text{ac,RMS}}$ is the root-mean-square (rms) of v_{ac}.

$$i_{pk1,\text{ideal}} \approx \frac{2v_{\text{ac}}P_{\text{dc}}}{V_{\text{ac,RMS}}^2}. \tag{41}$$

The disturbed current $i_{\text{val2}}(n)$ charges C_{oss} faster than $i_{\text{val2,ideal}}$. The time difference is

$$\Delta t(n) = \frac{1}{\omega_r}\left(\arctan\frac{Z_n i_{\text{val2,ideal}}}{v_{\text{ac}}} - \arctan\frac{Z_n i_{\text{val2}}(n)}{v_{\text{ac}}} + \arctan\frac{Z_n i_{\text{val1}}(n)}{v_{\text{ac}} - v_{\text{dc}}} - \arctan\frac{Z_n i_{\text{val1,ideal}}}{v_{\text{ac}} - v_{\text{dc}}}\right). \tag{42}$$

At the end of $T_{d,r}$, the disturbed current $i_{L,\text{dist}}$ may cross zero. Since the GaN 2DEG is not conducted, the disturbed inductor current cannot be positive.

$$i_{L,\text{dist}} = \begin{cases} i_{\text{val2}}(n) + \Delta t(n)\frac{v_{\text{ac}}}{L}, & \Delta t(n) < -\frac{i_{\text{val2}}(n)L}{v_{\text{ac}}} \\ 0, & \Delta t(n) \geq -\frac{i_{\text{val2}}(n)L}{v_{\text{ac}}}. \end{cases} \tag{43}$$

The actual current $i_{pk1}(n+1)$ is yielded as

$$i_{pk1}(n+1) = -i_{\text{val2,ideal}} + i_{L,\text{dist}}(n) + i_{pk1,\text{ideal}} \tag{44}$$

$i_{pk2}(n+1)$ is

$$i_{pk2}(n+1) = \sqrt{2K_1 + i_{pk1}^2(n+1)}. \tag{45}$$

Ideally, $i_{pk2,\text{ideal}}$ is

$$i_{pk2,\text{ideal}} = \sqrt{2K_1 + i_{pk1,\text{ideal}}^2}. \tag{46}$$

The SR turning-OFF current by iterative error at the next switching cycle is

$$i_{\text{val1}(n+1)} = i_{pk2}(n+1) - i_{pk2,\text{ideal}} + i_{\text{val1,ideal}}. \tag{47}$$

In Fig. 11(a), the ratio of $i_{\text{val1}}(n+1)/i_{\text{val1}}(n)$ is plotted. The blue zone is the natural ZVS case without SR extended conduction. The green zone is the ZVS with SR extension. The yellow zone is ZVS with SR preturning OFF. The red zone is the valley-switching case. Except for the green zone, the ratio is below unity, which means that the disturbance will be damped. In the green zone, the ratio increases to unity as the v_{ac} increases. This indicates that the disturbance damping performance at the ZVS extension case degrades as the v_{ac} increases. To better illustrate it, in Fig. 11(b), the ratio of $i_{\text{val1}}(n+1)/i_{\text{val1,ideal}}$ in the ZVS extension case is plotted. The ratio is greater than unity, which means that the disturbance will be accumulated at the next switching cycles and make $i_{L,\text{est}}$ lose tracking of i_L. On the other hand, in the valley-switching case, the disturbance damped to zero at the next switching cycle. For the conventional ZCD-circuit-based design, ZVS extension can achieve full load range ZVS, and the disturbance will be eliminated with the ZCD signal. In contrast, for the proposed current estimator-based control, no ZCD signal is available. For the ZVS extension case,

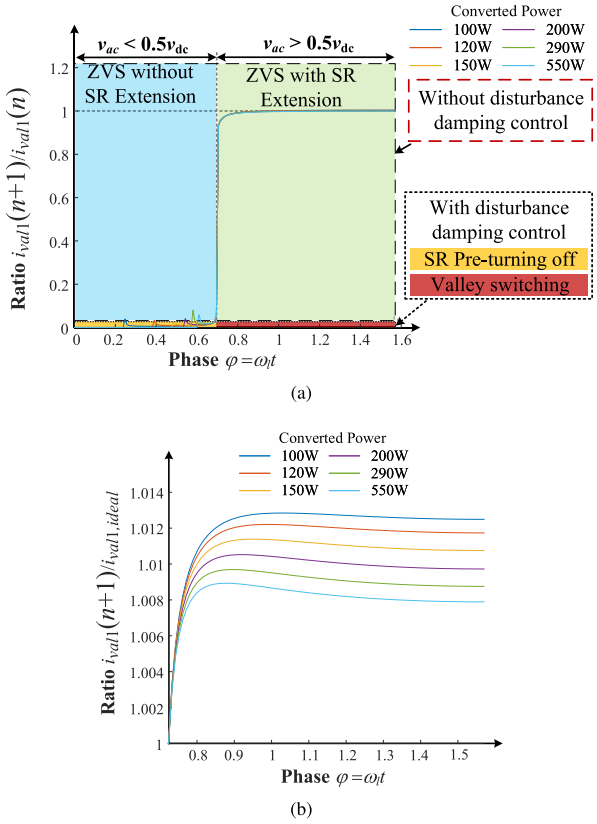

Fig. 11. Ratio of (a) $i_{\text{val1}}(n+1)/i_{\text{val1}}(n)$ and (b) ZVS extension case $i_{\text{val1}}(n+1)/i_{\text{val1,ideal}}$ under different loads.

it needs a disturbance observer [34] to eliminate the disturbance effect, which complicates the design. Valley switching simplifies the control algorithm with dead-beat disturbance-damping performance.

The proposed disturbance damping control consists of SR preturning OFF and valley switching. It alternates the SR conduction time. By preturning off the SR switch at $i_{L,\text{est}}$ zero-crossing point, no additional negative current will be injected into the inductor current. SR is preturned off before $i_{L,\text{est}}$ zero-crossing when $v_{\text{ac}} \leq 0.5\text{vdc}$. When $v_{\text{ac}} > 0.5v_{\text{dc}}$, valley switching is realized. Therefore, $i_{\text{val},1}$ is always zero in the whole line period.

To realize the proposed disturbance damping control, k_{po} is defined as the conduction ratio of the SR MOSFET turning-ON time. T_{SR} is

$$T_{\text{SR}} = \left(\frac{i_{L,\text{est}}(t_2)L}{v_{\text{dc}} - v_{\text{ac}}} - T_{d,f} + T_{\text{res},1} \right) k_{\text{po}}. \tag{48}$$

The SR ON-time is alternated. To keep the switching frequency unchanged, $T_{d,r}$ should be extended

$$T_{d,r} = \begin{cases} T_{\text{res},2} + \dfrac{L\sqrt{-2K_1}}{v_{\text{ac}} + V_D} \\ \quad + T_{\text{SR}} \dfrac{1 - k_{\text{po}}}{k_{\text{po}}}, & K_1 \leq 0 \text{ and } i_{L,\text{est}}(t_2) > 0 \\ \dfrac{v_{\text{ac}}}{v_{\text{ac}} + V_D} T_{\text{on}}, & K_1 \leq 0 \text{ and } i_{L,\text{est}}(t_2) = 0 \\ \dfrac{\pi}{\omega_n} + T_{\text{SR}} \dfrac{1 - k_{\text{po}}}{k_{\text{po}}}, & K_1 > 0. \end{cases} \tag{49}$$

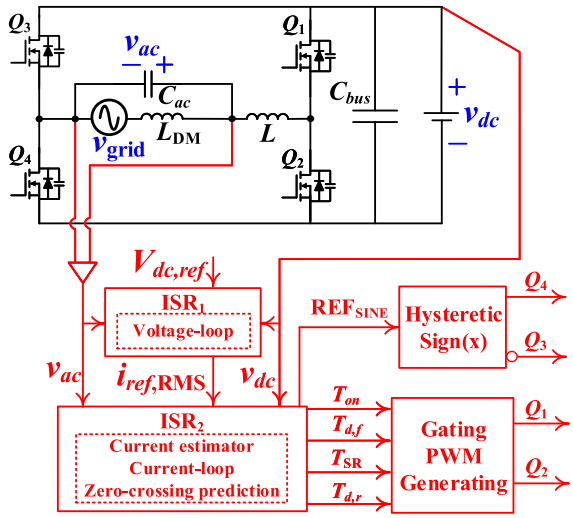

Fig. 12. Block diagram of the proposed controller.

In summary, with the proposed disturbance damping control, if a certain negative current is induced by disturbance, preturning OFF SR near the inductor current zero-crossing point can suppress the estimator error. Since the inductor current is near zero, the increased conduction loss is trivial.

B. System Implementation

The block diagram of the proposed controller is illustrated in Fig. 12. To attenuate the injection of the differential mode i_L into the grid, an *LC* filter that consists of C_{ac} and L_{DM} is added. There are two interrupt service routines (ISR_1, ISR_2) running at 10˜Hz and 40kHz, respectively. Gating signals for Q_1 and Q_2 are generated with given time parameters T_{on}, $T_{d,f}$, T_{SR}, and $T_{d,r}$.

The signals to be sampled and connected to the peripheral of the DSP in the proposed methodology includes input voltage v_{ac} and output voltage v_{dc}. In Fig. 12, v_{ac} and v_{dc} are sampled and fed into the controller with the generated PWM parameters, including ON-time, deadband, and SR time. The current estimator rebuilds the inductor current at the switching transition instants. Moreover, the inductor's current zero-crossing point can be predicted with the current estimator. Therefore, no inductor current sampling is required. It is also the highlight of the proposed method.

To send the two voltage signals of the power circuit to the DSP, a signal acquisition circuit is designed as shown in Fig. 13. First, the voltage on the power circuit would pass through a voltage divider with a low pass filter. The low-pass filter is used to filter the sensing noise. Then, a voltage follower buffers the voltage signal and sends it to the DSP ADC.

Function blocks of ISRs are presented in Fig. 14.

ISR_1 is in charge of low bandwidth algorithms, such as the calculation of the rms of the ac side voltage and PFC voltage-loop compensation. v_{ac}'s peak voltage is detected. Then, the rms voltage of the ac side $v_{\text{ac,RMS}}$ is obtained. The error between output voltage $V_{\text{dc,ref}}$ and the feedback dc-link voltage v_{dc} is fed to the voltage loop of the PI compensator. The compensator

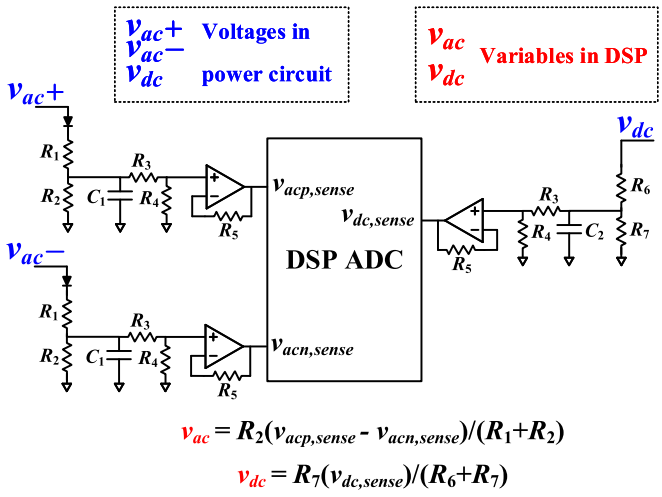

Fig. 13. Schematic of peripheral circuits to sample v_{ac} and v_{dc}.

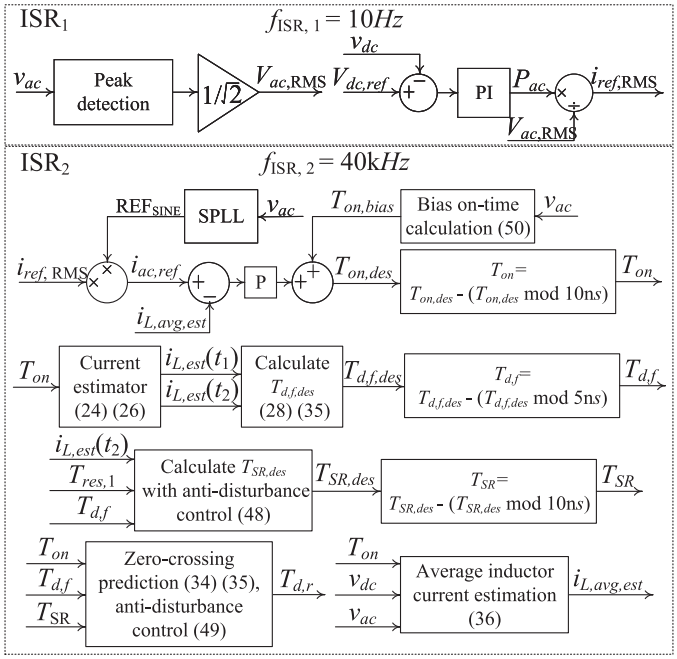

Fig. 14. Function details in ISR_1 and ISR_2.

gives the desired input power P_{ac}. Dividing P_{ac} by $v_{\text{ac,RMS}}$, the demanded rms current of ac side $i_{\text{ref,RMS}}$ can be obtained.

ISR_2 is in charge of algorithms such as software phase-lock-loop (SPLL) [35], estimator-based inner current loop, current zero-crossing prediction, and the averaged current estimator. SPLL generates a uniform sinusoidal signal REF_{sine} that is in phase with v_{ac}. The product of REF_{sine} and $i_{\text{ref,RMS}}$ provides the reference instantaneous input current $i_{\text{ac,ref}}$. In the inner current loop, the conventional current sensor is replaced with the proposed current estimator. Error between $i_{\text{ac,ref}}$ and $i_{L,\text{est}}$ is fed to a proportional unit. By adding a bias ON-time $T_{\text{on,bias}}$, the desired ON-time $T_{\text{on,des}}$ is determined. $T_{\text{on,des}}$ leads the average inductor current to follow the desired waveform $i_{\text{ac,ref}}$. $T_{\text{on,bias}}$

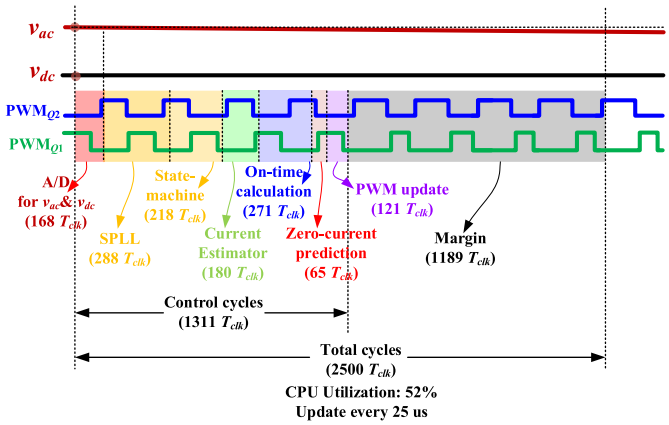

Fig. 15. DSP clock cycles of code computation and execution with the proposed zero-current predicting algorithm.

is the bias ON-time. The proportional controller is the tradeoff between the control accuracy and the response speed of $T_{\text{on,des}}$. $i_{L,\text{est}}$ is not equal to $i_{\text{ac,ref}}$ all the line cycle. There is a round-off error due to the discrete characteristic of DSP. For example, $T_{\text{on,bias}}$ may be calculated as 733 ns. However, the DSP can only generate a PWM waveform with ON-time 730 ns. This means the actual T_{on} has a minor deviation (within 10 ns) compared with the biased ON-time $T_{\text{on,bias}}$. It results that $i_{L,\text{est}}$ would be a bit different from $i_{\text{ac,ref}}$. Adding a compensator can mitigate the difference. A PI compensator has good accuracy. However, it may incur oscillation with improper parameters and increase the THD. Since the difference is trivial, the proportional controller with fast response and no oscillation can be used.

Since nonpower transfer scenario does not deliver real power, $T_{\text{on,bias}}$ is derived from the normal power transfer scenario.

$$T_{\text{on,bias}} = \frac{2Z_n L i_{\text{ac,ref}} + L(v_{\text{dc}} - v_{\text{ac}})}{v_{\text{ac}} Z_n} \tag{50}$$

where $T_{\text{on,des}}$ is a float number, and it may not be integer times of PWM resolution time (10ns for PWM counter and 5ns for deadband blocks). Considering the discretizing process of a digital system, the executed ON-time T_{on} is estimated. Using the executed ON-time in the current estimator reduces the error induced by discretizing in digital control. The process is similar for the desired deadband $T_{d,f,\text{des}}$ and desired SR ON-time $T_{\text{SR,des}}$.

$$\begin{aligned} T_{\text{on}} &= T_{\text{on,des}} - (T_{\text{on,des}} \bmod 10\text{ns}) \\ T_{d,f} &= T_{d,f,\text{des}} - (T_{d,f,\text{des}} \bmod 5\text{ns}) \\ T_{\text{SR}} &= T_{\text{SR,des}} - (T_{\text{SR,des}} \bmod 10\text{ns}). \end{aligned} \tag{51}$$

Also, the process in (51) is to achieve a more accurate $T_{d,r}$ and $T_{d,r}$ does not need to do that estimation. Finally, the averaged inductor current under the given T_{on}, v_{dc}, and v_{ac} are estimated. It will be fed into the current loop in the next execution of ISR_2.

Fig. 15 gives the DSP clock cycles of code computation and execution. At the beginning of an iteration, sampling and filtering of v_{ac} and v_{dc} take about 168 clock cycles (T_{clk}). Then, it takes 288 T_{clk} for SPLL to generate the reference sinusoidal signal (REF_{SINE}). With REF_{SINE}, the state machine

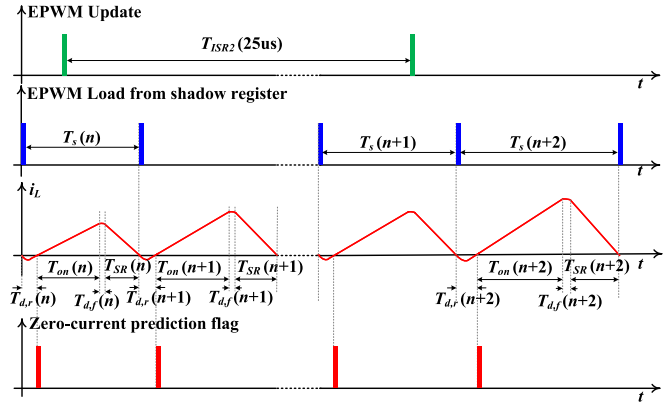

Fig. 16. Inductor current zero-crossing versus zero-current prediction between two different switching cycles.

TABLE II
DESIGN PARAMETERS

Parameters	Value
L	30 μH
Q_1, Q_2	LMG3410R070
Q_3, Q_4	IPW60R180P7
Rated output voltage v_{dc}	$400V$
Rated ac input v_{ac}	$220V_{\rm rms}$
Rated power	$550W$
C_{bus}	$1.2{\rm m}F$
Switching frequency range	$150{\rm k}Hz$-$1.6{\rm M}Hz$

determines whether to turn ON Q_3, Q_4 in 218 $T_{\rm clk}$. Next, the current estimator is executed with the previous ON/OFF time in 180 $T_{\rm clk}$. ON-time calculation is alternated with the estimated averaged inductor current in 271 $T_{\rm clk}$. Zero-crossing prediction is executed in 65 $T_{\rm clk}$. Consequently, PWM parameters are updated in another 121 $T_{\rm clk}$. The entire control process takes 1311 $T_{\rm clk}$. Meanwhile, certain redundancy should be reserved for other tasks. In our design, 1189 $T_{\rm clk}$ is reserved for each iteration, which corresponds to 52% CPU utilization.

In Fig. 16, the relationship between inductor current zero-crossing and the zero-current prediction between two different switching cycles is illustrated. The $\rm ISR_2$ predicts the inductor current zero-crossing point every 25 μs as shown in Fig. 15. When the prediction is updated, the flag EPWM Update is triggered. The shadow register of EPWM module is updated with $T_{\rm on}(n+1)$, $T_{d,r}(n+1)$, $T_{\rm SR}(n+1)$, $T_{d,f}(n+1)$. At the next PWM switching cycle, the data in the shadow register is loaded into the active register. The zero current is predicted on the turning-ON instant of Q_2 for the positive half line cycle and Q_1 for the negative half line cycle.

V. EXPERIMENTAL RESULTS

As a proof of concept, a 550-W-rated 220˜V to 400˜V, totem pole Boost PFC converter prototype is designed. The key design parameters are summarized in Table II. The photograph of the test bench is given in Fig. 17. TMS320F280049 C from Texas Instruments is used to implement the digital control algorithms. GaN devices with integrated gate drivers are used for the high-speed half bridge. The peak switching frequency is 1.6MHz. In

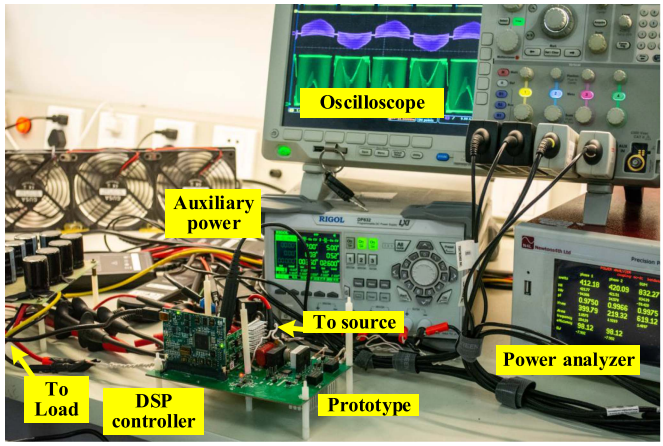

Fig. 17. Picture of the laboratory test bench.

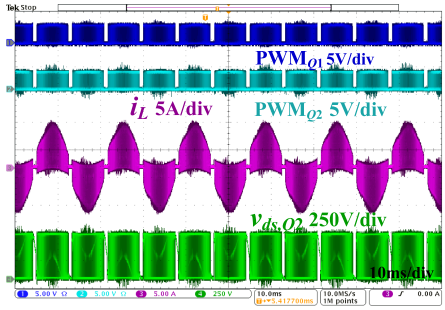

(a)

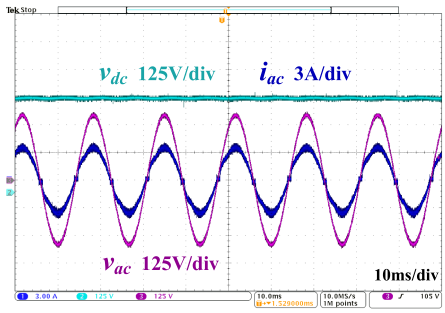

(b)

Fig. 18. Key waveforms under 220-V line input and 400-V DC output at full load. (a) Driving signals of $Q_{1,2}$, i_L, and $v_{\rm ds,Q2}$. (b) $v_{\rm ac}$, $v_{\rm dc}$, and $i_{\rm ac}$.

the experimental setup, heat sinks aided by air cooling are used for cooling.

At full load, the steady-state experimental waveforms are captured in Fig. 18. Since $Q_{1,2}$ are GaN devices with integrated gate-drivers, no direct $v_{\rm gs}$ can be measured [36]. The time delay between $v_{\rm gs}$ and the driving signal is less than 20˜ns. In the experiment, PWM signals are used to identify the gate driving signals, $\rm PWM_{Q1}$ for $v_{\rm gs,Q1}$ and $\rm PWM_{Q2}$ for $v_{\rm gs,Q2}$. i_L is at the boundary of DCM/CCM with a small negative current. $v_{\rm ds,Q2}$ is measured. The envelope of $v_{\rm ds,Q2}$ is clear. Input ac current i_{ac} is in phase with the input ac voltage. Voltage of dc-link $v_{\rm dc}$ is monitored.

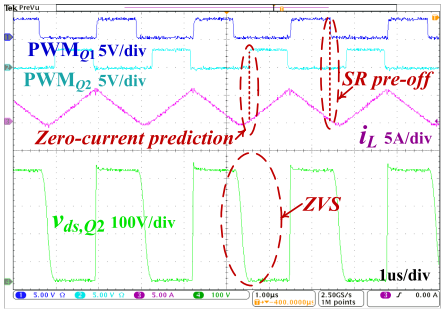

Fig. 19. ZVS waveforms when $v_{ac} < 0.5v_{dc}$ at full load.

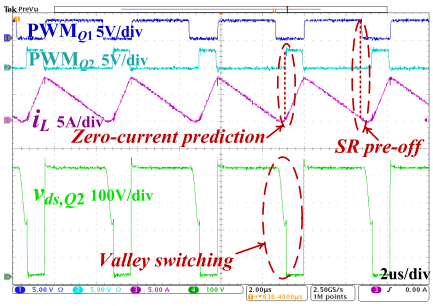

Fig. 20. Waveforms of valley switching when $v_{ac} > 0.5v_{dc}$ at full load.

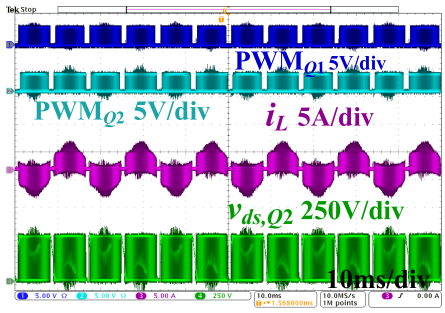

(a)

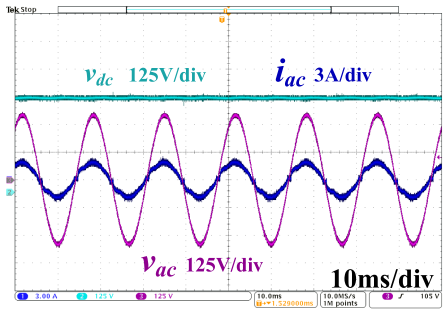

(b)

Fig. 21. Key waveforms under 220-V line input and 400-V DC output at half load. (a) Driving signals of $Q_{1,2}$, i_L, and $v_{ds,Q2}$. (b) v_{ac}, v_{dc}, and i_{ac}.

A zoom-in of Fig. 18 at positive v_{ac} is captured in Figs. 19 and 20. Fig. 19 demonstrates the ZVS when $v_{ac} < 0.5v_{dc}$. Fig. 20 captures the valley switching when $v_{ac} > 0.5v_{dc}$. Zero-current prediction is validated in both scenarios. The gating signal of Q_1 falls before i_L crosses zero. This validates the effectiveness of the proposed disturbance-damping control.

In Fig. 21, the steady-state experimental waveforms are captured at half load. i_L is at the boundary of DCM/CCM with a small negative current. The envelope of $v_{ds,Q2}$ is clear. i_{ac} is in phase with the input ac voltage. The ripple voltage of v_{dc} is smaller than that in full load condition.

Figs. 22 and 23 capture the zoom-in of Fig. 21 at positive v_{ac}. Fig. 22 monitored the ZVS when $v_{ac} < 0.5v_{dc}$. Fig. 23 demonstrates the valley switching when $v_{ac} > 0.5v_{dc}$. In both scenarios, zero-current prediction is validated. With the proposed disturbance damping control, the gate signal of Q_1 falls before i_L crosses zero.

Near zero-crossing of v_{ac}, the desired average current is relatively small and v_{ac} changes rapidly. Moreover, the converter's boost ratio is very high, which brings a large duty cycle and a small switching period. In this situation, the influence of control delay on the estimated current becomes significant. This may lead to a loss of tracking of the estimator and additional THD. Therefore, both Q_1 and Q_2 remain off in a no-switching state and the inductor current stays zero when v_{ac} is near zero crossing. Since the duration of the no-switching zone is short compared with the whole line cycle (less than 5%), and the desired averaged current in this zone is also small, the harmonic components introduced by the no-switching zone are high order, low amplitude. The impact on THD by the no-switching state is trivial.

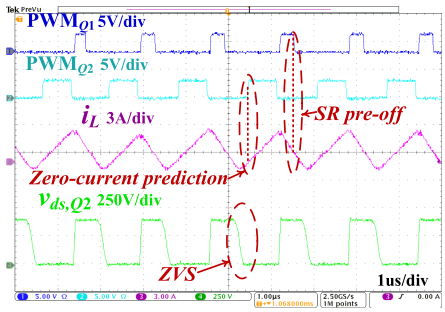

Fig. 22. ZVS waveforms when $v_{ac} < 0.5v_{dc}$ at half load.

The harmonic components of i_{ac} at 550-W output power (full load) are plotted in Fig. 24. The harmonic components are lower than 3.6% of the fundamental component.

The input current THD (iTHD) is measured at different output power. The results are recorded in Fig. 25. The lowest iTHD is 5.4% at 427-W output power.

The power factor correction performance under different load conditions is presented in Fig. 26. Correspondingly, Fig. 27 demonstrates the efficiency trend. As shown, the designed prototype exhibits 98.96% peak efficiency with 0.9972 power factor. As shown, high efficiency and high power factor are maintained over a wide load range.

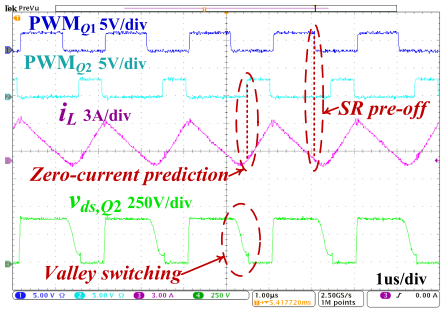

Fig. 23. Waveforms of valley switching when $v_{ac} > 0.5v_{dc}$ at half load.

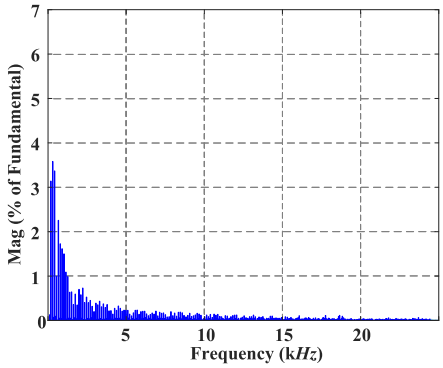

Fig. 24. FFT analysis with 220-V AC input, 400-V DC output, full load (550 W) condition.

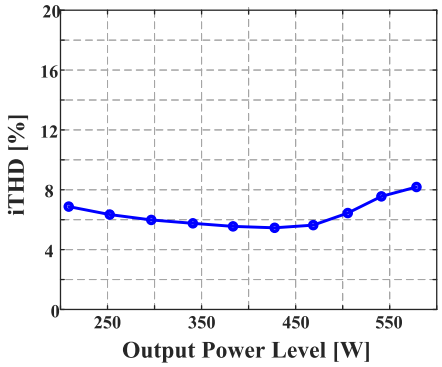

Fig. 25. Measured iTHD versus output power under 220-V AC input.

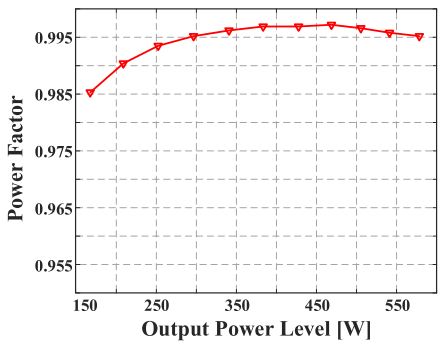

Fig. 26. Measured power factor versus output power.

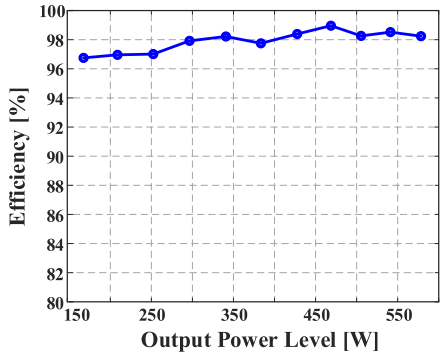

Fig. 27. Measured efficiency versus output power.

VI. Conclusion

In this article, a novel current sensorless CRM control is proposed for totem-pole Boost PFC converters. It utilizes an inductor current estimator model to estimate the averaged current and to predict the current zero crossings. Compared with the conventional methods, the inductor current sensing signal and the zero-current detecting circuit are no longer required. The control loop and the peripheral circuit are simplified. The behavior of the estimator considering switching device C_{oss} model is analyzed and detailed. A disturbance damping control is proposed to mitigate the variation of inductance and parasitic resistance and improve the prediction accuracy. The operation principles, digital implementation, and estimation error suppression are discussed.

The proposed concept is verified in a 550-W-rated experimental prototype. With the proposed control scheme, the zero-crossing point of the inductor current is predicted. Valley-switching and zero-voltage switching are realized at the predicted zero-crossing points. The experiment results exhibit 98.96% peak efficiency with 0.9972 power factor. Good power factor and efficiency performances are achieved over a wide load range.

References

[1] H. Wang and A. Khaligh, "Interleaved SEPIC PFC converter using coupled inductors in PEV battery charging applications," in *Proc. IEEE Appl. Power Electron. Conf. Expo.*, 2015, pp. 586–591.

[2] L. Huber, Y. Jang, and M. M. Jovanovic, "Performance evaluation of bridgeless PFC boost rectifiers," *IEEE Trans. Power Electron.*, vol. 23, no. 3, pp. 1381–1390, May 2008.

[3] Q. Huang and A. Q. Huang, "Review of GaN totem-pole bridgeless PFC," *CPSS Trans. Power Electron. Appl.*, vol. 2, no. 3, pp. 187–196, 2017.

[4] K. Zhu, A. Bhalla, and J. Dodge, "Enabling 99.3% efficiency in 3.6 kW totem-pole PFC using new 750 V Gen 4 SiC FETs," *IEEE Power Electron. Mag.*, vol. 8, no. 4, pp. 30–37, Dec. 2021.

[5] M. Zhou, L. Yu, and H. Wang, "A SiC-based highly integrated bidirectional ac/dc converter for PEV charging applications," in *Proc. IEEE Int. Power Electron. Appl. Symp.*, 2021, pp. 1–5.

[6] L. Li et al., "Maximum efficiency average current controller based on a comprehensive charge rate model for DCM boost PFC converter," *IEEE Trans. Power Electron.*, vol. 36, no. 5, pp. 6046–6055, May 2021.

[7] C. Zhao and X. Wu, "Accurate operating analysis of boundary mode totem-pole boost PFC converter considering the reverse recovery of MOSFET," *IEEE Trans. Power Electron.*, vol. 33, no. 12, pp. 10038–10043, Dec. 2018.

[8] Y. Jia et al., "Characterization and optimal control of totem-pole PFC converter with high frequency GaN HEMTs and low frequency Si diodes," *IEEE Trans. Ind. Electron.*, vol. 68, no. 11, pp. 10740–10749, Nov. 2021.
[9] R. Min, G. Shen, Q. Tong, Q. Zhang, H. Peng, and X. Zou, "Unified pulsewidth-cycle control strategy to achieve mixed DCM/CRM operation and consistent valley switching for boost PFC converter," *IEEE Trans. Power Electron.*, vol. 36, no. 11, pp. 13304–13316, Nov. 2021.
[10] B. Su, J. Zhang, and Z. Lu, "Totem-pole boost bridgeless PFC rectifier with simple zero-current detection and full-range ZVS operating at the boundary of DCM/CCM," *IEEE Trans. Power Electron.*, vol. 26, no. 2, pp. 427–435, Feb. 2011.
[11] C. Marxgut, F. Krismer, D. Bortis, and J. W. Kolar, "Ultraflat interleaved triangular current mode (TCM) single-phase PFC rectifier," *IEEE Trans. Power Electron.*, vol. 29, no. 2, pp. 873–882, Feb. 2014.
[12] Z. Liu, Z. Huang, F. C. Lee, and Q. Li, "Digital-based interleaving control for GaN-based MHz CRM totem-pole PFC," *IEEE J. Emerg. Sel. Topics Power Electron.*, vol. 4, no. 3, pp. 808–814, Sep. 2016.
[13] Q. Huang, R. Yu, Q. Ma, and A. Q. Huang, "Predictive ZVS control with improved ZVS time margin and limited variable frequency range for a 99% efficient, 130-w/in3 MHz GaN totem-pole PFC rectifier," *IEEE Trans. Power Electron.*, vol. 34, no. 7, pp. 7079–7091, Jul. 2019.
[14] K. Yao et al., "Optimal switching frequency variation range control for critical conduction mode boost power factor correction converter," *IEEE Trans. Power Electron.*, vol. 68, no. 2, pp. 1197–1209, Feb. 2021.
[15] D. Shahzad, S. Pervaiz, N. A. Zaffar, and K. K. Afridi, "GaN-based high-power-density AC-DC-AC converter for single-phase transformer-less online uninterruptible power supply," *IEEE Trans. Power Electron.*, vol. 36, no. 12, pp. 13968–13984, Dec. 2021.
[16] L. Li, Q. Zhang, R. Min, K. Liu, Q. Tong, and D. Lyu, "A current reshaping strategy to reduce parasitics-induced current distortion in discontinuous conduction mode boost power factor correction converter," *IEEE Trans. Ind. Electron.*, vol. 68, no. 3, pp. 2215–2224, Mar. 2021.
[17] J. Sun, N. N. Strain, D. J. Costinett, and L. M. Tolbert, "Analysis of a GaN-based CRM totem-pole PFC converter considering current sensing delay," in *Proc. IEEE Energy Convers. Congr. Expo*, 2019, pp. 4421–4428.
[18] X. Ren, Y. Zhou, Z. Guo, Y. Wu, Z. Zhang, and Q. Chen, "Simple analog-based accurate variable on-time control for critical conduction mode boost power factor correction converters," *IEEE J. Emerg. Sel. Topics Power Electron.*, vol. 8, no. 4, pp. 4025–4036, Dec. 2020.
[19] D. Rahman, M. A. Awal, M. S. Islam, W. Yu, and I. Husain, "Low-latency high-speed saturable transformer based zero-crossing detector for high-current high-frequency applications," in *Proc. IEEE Energy Convers. Congr. Expo.*, 2020, pp. 3266–3272.
[20] G. Schrom, R. S. Vunnam, S. Makala, and A. Lyakhov, "High-speed ZVS-ZCS soft-switching CMOS bridge drivers for a DC-DC fully integrated voltage regulator (FIVR) operating at 100–320 MHz on 22 nm process node," in *Proc. IEEE Appl. Power Electron. Conf. Expo.*, 2019, pp. 2263–2267.
[21] K. Wang, H. Zhu, J. Wu, X. Yang, and L. Wang, "Adaptive driving scheme for ZVS and minimizing circulating current in MHz CRM converters," *IEEE Trans. Power Electron.*, vol. 36, no. 4, pp. 3633–3637, Apr. 2021.
[22] M. Torrisi, S. Messina, and M. Cacciato, "Hysteresis current control for a high efficiency totem pole PFC in zero voltage switching," in *Proc. Eur. Conf. Power Electron. Appl.*, 2021, pp. P.1–P.10.
[23] X. Chen, G. Son, F. Jin, and Q. Li, "A microcontroller-based high efficiency critical conduction mode control for GaN-based totem-pole PFC," in *Proc. IEEE Workshop Control Model. Power Electron.*, 2021, pp. 1–7.
[24] J. Chen, W. Tai, B. Xun, C. Gong, and J. Chen, "Improved control strategies for totem-pole PFC with true full range ZVS operation," *IEEE Trans. Ind. Electron.*, vol. 70, no. 3, pp. 2419–2430, Mar. 2023.
[25] H. Xi, L. Li, G. Xu, and M. Su, "SiC-based high-frequency soft-switching interleaved totem-pole bridgeless PFC converter without ZCD circuits," in *Proc. IEEE Int. Power Electron. Appl. Symp.*, 2021, pp. 1–5.
[26] Z. Wang, S. Wang, P. Kong, and F. C. Lee, "DM EMI noise prediction for constant on-time, critical mode power factor correction converters," *IEEE Trans. Power Electron.*, vol. 27, no. 7, pp. 3150–3157, Jul. 2012.
[27] H.-C. Chen, C.-Y. Lu, G.-T. Li, and W.-C. Chen, "Digital current sensorless control for dual-boost half-bridge PFC converter with natural capacitor voltage balancing," *IEEE Trans. Power Electron.*, vol. 32, no. 5, pp. 4074–4083, May 2017.
[28] F. Lopez, V. M. Lopez-Martin, F. J. Azcondo, L. Corradini, and A. Pigazo, "Current-sensorless power factor correction with predictive controllers," *IEEE J. Emerg. Sel. Topics Power Electron.*, vol. 7, no. 2, pp. 891–900, Jun. 2019.
[29] A. Chandwani, S. Dey, and A. Mallik, "Parameter variation tolerant robust current sensorless control of a single-phase boost PFC," *IEEE J. Emerg. Sel. Topics Ind. Electron*, vol. 3, no. 4, pp. 933–945, Oct. 2022.
[30] M. Kasper, R. M. Burkart, G. Deboy, and J. W. Kolar, "ZVS of power MOSFETs revisited," *IEEE Trans. Power Electron.*, vol. 31, no. 12, pp. 8063–8067, Dec. 2016.
[31] D. Costinett, D. Maksimovic, and R. Zane, "Circuit-oriented treatment of nonlinear capacitances in switched-mode power supplies," *IEEE Trans. Power Electron.*, vol. 30, no. 2, pp. 985–995, Feb. 2015.
[32] L. Huber, B. T. Irving, and M. M. Jovanovic, "Effect of valley switching and switching-frequency limitation on line-current distortions of DCM/CCM boundary boost PFC converters," *IEEE Trans. Power Electron.*, vol. 24, no. 2, pp. 339–347, Feb. 2009.
[33] R. Hou, J. Lu, and D. Chen, "Parasitic capacitance EQOSS loss mechanism, calculation, and measurement in hard-switching for GaN HEMTs," in *Proc. IEEE Appl. Power Electron. Conf. Expo.*, 2018, pp. 919–924.
[34] W.-H. Chen, J. Yang, L. Guo, and S. Li, "Disturbance-observer-based control and related methods–An overview," *IEEE Trans. Ind. Electron.*, vol. 63, no. 2, pp. 1083–1095, Feb. 2016.
[35] F. D. Freijedo, A. G. Yepes, Ó. López, P. Fernandez-Comesana, and J. Doval-Gandoy, "An optimized implementation of phase locked loops for grid applications," *IEEE Trans. Instrum. Meas.*, vol. 60, no. 9, pp. 3110–3119, Sep. 2011.
[36] G. Tang et al., "High-speed, high-reliability GaN power device with integrated gate driver," in *Proc. IEEE Int. Symp. Power Semicond. Devices IC's*, 2018, pp. 76–79.

Mingde Zhou (Student Member, IEEE) received the B.S. degree in automation from Shandong University, Jinan, China, in 2019. He is currently working toward the Ph.D. degree in electrical engineering with the School of Information Science and Technology, ShanghaiTech University, Shanghai, China.

His research interests include ac/dc bidirectional converters, wide gain range resonant converters, and bidirectional dc–dc converters.

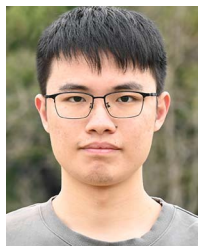

Chuhan Peng (Student Member, IEEE) received the B.S. degree in electrical engineering from Zhejiang University, Hangzhou, China, in 2022. He is currently working toward the master's degree in electrical engineering with the School of Information Science and Technology, Shanghaitech University, Shanghai, China.

His current research interests include ultrawide voltage range bidirectional dc–dc converters.

Junrui Liang (Senior Member, IEEE) received the Ph.D. degree in mechanical and automation engineering from The Chinese University of Hong Kong (CUHK), Hong Kong, in 2010.

Since November 2013, he has been with the School of Information Science and Technology, ShanghaiTech University, Shanghai, China, as an Assistant Professor. His most significant contribution was that he extended the impedance modeling and analysis, which conventionally was only used for linear systems, to some nonlinear power conversion systems such as the class-E power amplifier and piezoelectric energy harvesting systems. His recent research interests include dynamics of nonlinear electromechanical coupling systems, kinetic energy harvesting and vibration control, electrical power conversion and utilization research, renewable energy, etc.

Minfan Fu (Senior Member, IEEE) received the B.S., M.S., and Ph.D. degrees in electrical and computer engineering from the University of Michigan Shanghai Jiao Tong University Joint Institute, Shanghai Jiao Tong University, Shanghai, China, in 2010, 2013, and 2016, respectively.

From 2016 to 2018, he held a postdoctoral position with the Center for Power Electronics Systems (CPES), Virginia Polytechnic Institute and State University, Blacksburg, VA, USA. He is currently an Assistant Professor with the School of Information Science and Technology, ShanghaiTech University, Shanghai, China. He holds one U.S. patent, seven Chinese patents, and has authored or co-authored more than 80 papers in prestigious IEEE journals and conferences. His research interests include megahertz wireless power transfer, high-frequency power conversion, high-frequency magnetic design, and application of widebandgap devices.

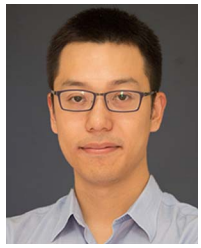

Haoyu Wang (Senior Member, IEEE) received the bachelor degree with distinguished honor from Zhejiang University, Hangzhou, China, in 2009, and the Ph.D. degree from the University of Maryland, College Park, MD, USA, in 2014, both in electrical engineering.

In September 2014, he joined the School of Information Science and Technology, ShanghaiTech University, Shanghai, China, where he is currently an Associate Professor with tenure. His research interests include power electronics, plug-in electric and hybrid electric vehicles, the applications of wide bandgap semiconductors, renewable energy harvesting, and power management integrated circuits.

Dr. Wang is an Associate Editor for IEEE TRANSACTIONS ON INDUSTRIAL ELECTRONICS, IEEE TRANSACTIONS ON TRANSPORTATION ELECTRIFICATION, and *CPSS Transactions on Power Electronics and Applications*.